

The cation-vacancy ordering transition in dehydrated Na₆ sodalite

Branton J. Campbell, J. Miguel Delgado, Anthony K. Cheetham, Bo B. Iversen, Nick P. Blake, Scott R. Shannon, Susan Lattner, and Galen D. Stucky

Citation: *The Journal of Chemical Physics* **113**, 10226 (2000); doi: 10.1063/1.1319351

View online: <http://dx.doi.org/10.1063/1.1319351>

View Table of Contents: <http://scitation.aip.org/content/aip/journal/jcp/113/22?ver=pdfcov>

Published by the [AIP Publishing](#)



Re-register for Table of Content Alerts

Create a profile.



Sign up today!



The cation-vacancy ordering transition in dehydrated Na₆ sodalite

Branton J. Campbell,^{a)} J. Miguel Delgado,^{b)} and Anthony K. Cheetham

Materials Research Laboratory and Materials Department, University of California, Santa Barbara, California 93106

Bo B. Iversen,^{c)} Nick P. Blake, Scott R. Shannon, Susan Lattner, and Galen D. Stucky

Chemistry Department, University of California, Santa Barbara, California 93106

(Received 30 June 2000; accepted 29 August 2000)

Variable-temperature synchrotron x-ray powder diffraction data from dehydrated Na₆[Al₆Si₆O₂₄] reveal a structural phase transition that involves both the commensurate ordering of the extra-framework Na cations and a one-dimensional incommensurate modulation of the framework. Peak splittings and superlattice reflections implicate an orthorhombically-distorted volume-doubled supercell at room temperature ($a=12.9432$ Å, $b=12.8403$ Å, and $c=9.1372$ Å) $\sim(\sqrt{2}a \times \sqrt{2}a \times a)$. These data also included additional superlattice peaks associated with an incommensurate long-period modulation with $\tau=(3/2 \ 1/2 \ 1)/8.9$. All unique orderings of the 12 Na cations among the 16 available sites of the commensurate supercell are enumerated. A unique solution is identified that minimizes the structural energy and accounts for the observed superlattice peaks. Rietveld analysis reveals a significant Pauling “partial-collapse” tilt angle in the cation-ordered phase, that appears to decrease with increasing temperature. © 2000 American Institute of Physics. [S0021-9606(00)00844-8]

I. INTRODUCTION

Sodalite materials, both natural and synthetic, vary widely in composition, the common structural theme being the sodalite framework. The sodalite cage, also called the “beta” cage, is a truncated octahedron, having six 4-ring faces and eight 6-ring faces.¹ These cages are stacked in a space-filling body-centered cubic arrangement, such that a cage shares a 6-ring face with each of its eight nearest neighbors along the $\langle 111 \rangle$ directions and a 4-ring face with each of its next nearest neighbors along the $\langle 100 \rangle$ directions. The vertices of the cage are tetrahedrally coordinated sites (T-sites) that are typically occupied by Si or Al atoms while the cage edges are bridging oxygen atoms. While natural sodalite minerals are technically classified as feldspathoids rather than zeolites due to their small pore sizes (~ 3 Å), the sodalite framework is typically discussed in connection with other zeolites because the sodalite cage is also a building block in other important zeolite frameworks such as LTA, EMT, and FAU.

Loewenstein’s rule² of aluminum avoidance in the aluminosilicate frameworks leads to a tendency for Al ordering so as to place Si and Al on crystallographically distinct sites. In an ordered framework, Si and Al sites can be readily distinguished due to their different T–O bond lengths (1.61 Å vs 1.74 Å, respectively). Typical aluminosilicate sodalites have compositions of the form

$M_m^{q+}[(Al_nSi_{12-n}O_{24})^{n-}]X_x^{r-}$, where $qm - rx = n$, so that extra-framework (EF) cations and anions serve to balance the charge of a non-neutral aluminosilicate framework. The charge-balancing cations (M^{q+}) are typically alkaline or alkaline earth metals and occupy sites near the centers of the 6-ring windows, coordinating to the six oxygens of the ring. Because the attraction to these window sites is strong, the most stable cation configurations coordinate one cation to each of the eight windows (e.g., $M_8^{2+}[Al_{12}O_{24}]X_2^{2-}$, $M_8^+[Al_6Si_6O_{24}]X_2^-$, and $M_8^+[Al_8Si_4O_{24}]$). When additional EF anions (X^{r-}) are present, such as Cl^- or OH^- or CrO_4^{2-} , they occupy sites at or near the centers of the sodalite cages and effectively form salt complexes with the EF cations. Sodalite compounds that contain no EF anions have been referred to as “salt-free.”³ In salt-free sodalites, overall charge-neutrality may require that some of the cation sites remain vacant, as is the case with $M_6^{2+}\square_2[Al_{12}O_{24}]$, $M_4^{3+}\square_4[Al_{12}O_{24}]$, and $M_6^+\square_2[Al_6Si_6O_{24}]$, where \square represents a vacancy. This work is primarily an investigation of low-temperature cation-vacancy ordering in dehydrated salt-free sodium sodalite, $Na_6\square_2[Al_6Si_6O_{24}]$ (referred to hereafter as Na₆–SOD), which has an ordered Si/Al=1 framework and one vacant cation site per sodalite cage (two per unit cell).

The sodalite framework is highly flexible and susceptible to several different types of framework distortion, the most well-known of which is the TO₄ tetrahedral “tilt,” which was referred to as “partial collapse” by Pauling in the first structure determination of mineral sodalite by single crystal x-ray diffraction.¹ The Pauling tilt angle reduces the volume of the unit cell by rotating each TO₄ tetrahedra by a small angle about one of its $\bar{4}$ axes. This rotation causes the three oxygens on one side of a 6-ring window to move to

^{a)} Author to whom correspondence should be addressed. Current address: Materials Science Division, Argonne National Laboratory, Argonne, Illinois 60439.

^{b)} Permanent address: Universidad de Los Andes, Department of Chemistry, Merida 5251, Venezuela.

^{c)} Current address: University of Aarhus, Department of Chemistry, Aarhus DK-8000, Denmark.

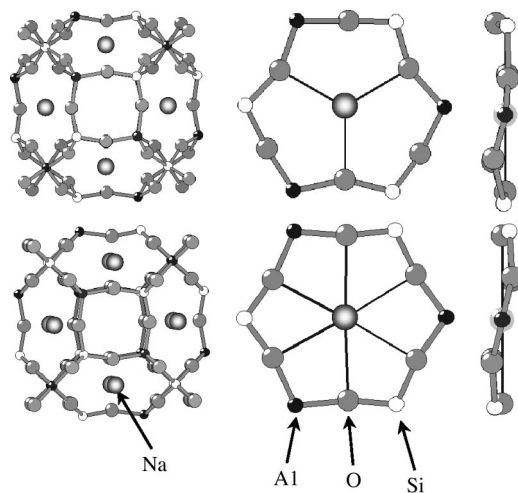


FIG. 1. An ordered alumino-silicate sodalite cage with and without significant Pauling tilt angle.

wards window-center and into the window plane while the three oxygens on the other side move out from window-center and further from the window plane (see Fig. 1). $\text{Na}_6\text{-SOD}$ exhibits a remarkable 9% volume increase upon removing H_2O from the cages of hydrated sample.^{4,5} The presence of the water partially shields each cation from the field generated by the other cations around the cage, thereby allowing each one to move further in towards the cage center, which is facilitated by a large Pauling tilt. EF anions also serve to shield cation-cation interactions as evidenced by the fact that several salt-bearing sodalites⁶⁻⁹ are reported to have smaller volumes than their salt-free counterparts, despite playing host to more EF atoms. Hassan and Grundy¹⁰ showed that separate Pauling tilt parameters can be defined for SiO_4 and AlO_4 tetrahedra in ordered alumino-silicate sodalites, and Depmeier¹¹ showed that sodalites can also experience a tetragonal distortion of the framework TO_4 tetrahedra, which tends to be most severe in the Al-rich compositions.

While these modes of framework distortion are widely observed, they are still fully compatible with cubic symmetry. $\text{Na}_6\text{-SOD}$, however, has been reported by Sieger¹² to deviate from cubic symmetry at low temperatures, experiencing a phase transition near 530 K that was accompanied by the appearance of superlattice reflections that resisted indexing. Because there can be no cubic arrangement of the two cation-site vacancies in each unit cell, any ordered vacancy arrangement is expected to result in a deviation from cubic symmetry and a response from the framework. Depmeier has also discussed the ordering of EF material (e.g., cation-vacancy ordering and orientational anion ordering) as a symmetry lowering influence capable of producing deviations from cubic symmetry in sodalites.¹³ For example, the dynamic orientational disorder of distorted WO_4^{2-} anions in $\text{Ca}_8[\text{Al}_{12}\text{O}_{24}](\text{WO}_4)_2$ stabilizes the cubic phase at high temperatures, whereas an orthorhombic distortion locks in at lower temperatures.¹⁴ In this work, low-temperature peak splittings and superlattice peaks are observed, indexed, and

used to refine a superstructure model obtained with the aid of computer simulations carried out by Shannon *et al.*¹⁵

II. EXPERIMENT

In order to investigate possible low-symmetry phases in $\text{Na}_6\text{-SOD}$, a sample was prepared hydrothermally, dehydrated, and then sealed in a capillary tube for synchrotron powder diffraction data collection. The intermediate product, $\text{Na}_8[\text{Al}_6\text{Si}_6\text{O}_{24}](\text{OH})_2 \cdot n\text{H}_2\text{O}$ (hydroxysodalite), was synthesized first from a basic solution of aluminum isopropoxide and tetraethylorthosilicate. First, 10.213 g of aluminum isopropoxide (0.050 mol; Strem Chemicals, 99.99%) and 40.0 g of NaOH (1.0 mol; Fisher Chemicals, 98.5%) were placed together in a Teflon autoclave liner with a magnetic stir bar. Water was added and the mixture stirred until the solids had completely dissolved. Next, 10.42 g of tetraethylorthosilicate (0.050 mol; Acros, 98%) was added dropwise while stirring, after which water was added until the Teflon vessel was 75% full. The Teflon liner was then sealed in a stainless steel Parr autoclave and placed in an oven at 180 °C for 10 days. The starting materials were specifically selected in order to avoid the incorporation of iron impurities into the product, a common problem for syntheses that use kaolin or alumina, and resulted in a smaller average particle size, which facilitated subsequent ion exchange.

Soxhlet extraction was then employed to remove NaOH from the hydroxysodalite resulting in nonbasic $\text{Na}_6[\text{Al}_6\text{Si}_6\text{O}_{24}] \cdot 8\text{H}_2\text{O}$ (hydrosodalite). The extent of extraction was monitored by x-ray powder diffraction and thermogravimetric analysis. When the XRD pattern indicated a full conversion to hydrosodalite, and TGA weight loss data showed no more sign of hydroxyl removal in the 700–800 °C range (water molecules in the cages are removed at 400 °C), the extraction was judged to be complete. The hydrosodalite was then placed in a schlenk flask and dried under vacuum at 10^{-5} torr while slowly ramping from room temperature to 430 °C over a period of 5 h, holding at 430 °C for another 5 h, and turning the oven off to cool. The flask was then closed and brought into an inert atmosphere dry box to avoid rehydration of the dry $\text{Na}_6\text{-SOD}$ powder. The sample was then sealed under dry argon in a 1.0 mm quartz capillary tube in order to maintain the dehydrated state.

Temperature resolved synchrotron powder diffraction measurements were carried out at beamline X7B at the National Synchrotron Light Source (NSLS) at Brookhaven National Laboratory ($\lambda=0.9341$ Å). Diffraction intensities were recorded on 200×400 mm Fuji image plates (IP) which were then scanned offline on a Fuji BAS2000 scanner with a pixel size of 0.1×0.1 mm. The data were recorded using the translating image plate method in which a narrow slice of the IP is exposed to the diffracted beam while the IP is moved. The movement of the plate was coupled to the sample temperature controller to yield a continuous variation of the diffraction pattern with temperature. Data collection was initiated at a sample temperature of 365 K which was then raised to 675 K in 195 min. At this point, the temperature was maintained at 675 K for 30 min, before the sample was allowed to cool to 365 K in 195 min. Heating was accomplished by placing a heating element close to the sample. A detailed description

of the X7B beam line characteristics and the experimental setup for IP x-ray powder diffraction measurements has been reported by Norby.¹⁶ The wavelength, detector distance, zero point, and IP tilt angle were determined by refining the diffraction pattern of a LaB₆ standard sample (NIST #660, $a = 4.15695 \text{ \AA}$). The data were corrected for Lorentz, polarization (95% polarized beam) and zero-point effects, and transformed to equivalent step size for further analysis. Rietveld refinements were performed on one-dimensional 393 K and 675 K powder patterns, which were prepared by averaging over 50 pixels along the temperature axis.

Because the (110) peak was much more intense than any other peak in the diffraction pattern, the IP translation speed, scanner sensitivity, and scanner dynamic range were selected so as to allow this peak to become saturated in order to gain needed sensitivity in the regions of the more subtle features of the pattern. An additional data set containing the full Debye–Scherrer cones on the IP was collected at 100 K for 1 h in which the (100) peak was not saturated. From this image, the central 50 pixels were used to produce a single high-sensitivity pattern.

A high-resolution room-temperature synchrotron powder diffraction pattern was also recorded at the NSLS beamline X7A at $\lambda = 1.1628 \text{ \AA}$ from $2\theta = 5^\circ$ to 65° in step-scan increments of 0.01° using a channel-cut double-crystal Ge(111) monochromator, a flat Ge(220) crystal analyzer, a NaI/Tl scintillation detector, sample rotation for better powder averaging, dead-time correction, normalization with respect to the incident beam intensity, and calibration with a Si standard. Counting times were increased at high angles and the intensities and estimated statistical errors were rescaled accordingly.

III. RESULTS AND DISCUSSION: POWDER INDEXING

A. An order–disorder phase transition

The variable-temperature synchrotron XRD data in Fig. 2 shows a nearly body-centered cubic pattern for Na₆-SOD in the high-temperature region. The presence of a small (210) peak and a barely perceptible (100) peak indicate that body-centering symmetry is slightly violated due to differentiation between Si and Al sites. The most intense peaks in the pattern are (110), (211), (310), (222), and (004). A phase transition is evident in several features of the diffraction data. First and most obvious are a series of new peaks, most quite small, that appear abruptly and reversibly near 510 K. Figure 3 was obtained by plotting the diffracted intensity at the top of the $2\theta = 7.2^\circ$ superlattice peak (peak A) vs temperature across the transition during both the heating and cooling cycles. While the powder diffraction data indicates a transition temperature of $510 \pm 10 \text{ K}$, subsequent differential scanning calorimetry (DSC) measurements on several similar samples suggest that the transition occurs near $535 \pm 5 \text{ K}$, which is in approximate agreement with the results of Sieger.¹² Because an error in the temperature calibration used for the powder diffraction measurements cannot be ruled out, the precise transition temperature remains an open question. On heating up through the transition, the DSC measurements revealed two endothermic peaks at 535 K and 553

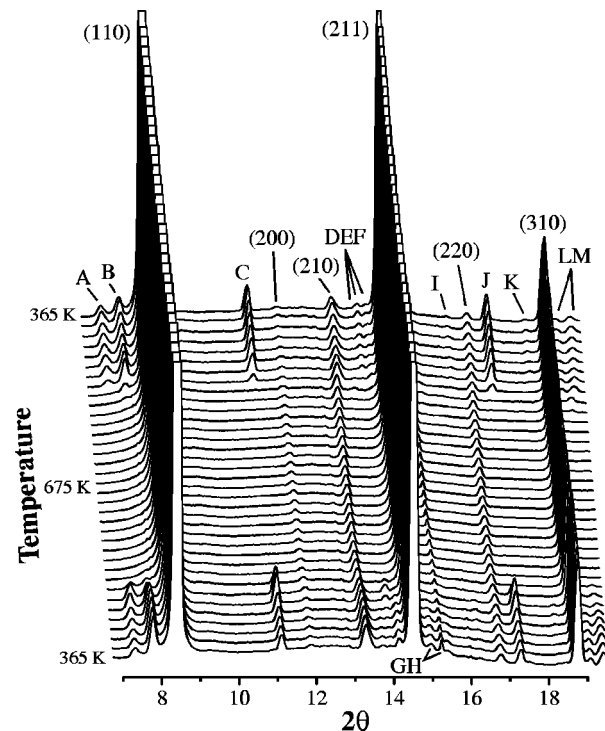


FIG. 2. Variable-temperature synchrotron XRD data for Na₆-SOD ($\lambda = 0.9341 \text{ \AA}$). The temperature ramps from 365 K to 675 K and back to 365 K. The intensity scale of the figure was selected so as to enhance the smaller peaks in the pattern, allowing only a partial view of the most intense peaks.

K. Upon recooling, however, only a single exothermic peak appeared at 535 K. Additional heating/cooling cycles reproduced the phenomenon, the energy of the 535 K transition being about 6 kJ/mol in each case. The satellite peak intensity in Fig. 3 does demonstrate different behaviors during heating and cooling, though no additional higher-temperature anomaly is evident during heating.

B. Peak splitting

A careful examination of the room-temperature synchrotron XRD data collected on beamline X7A revealed that

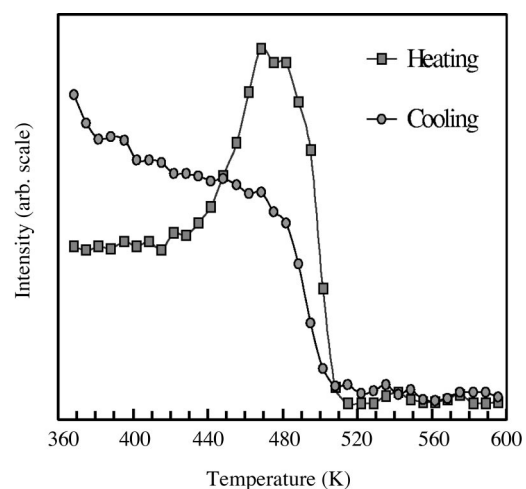


FIG. 3. Temperature dependence of the superlattice peak at $2\theta = 7.2^\circ$ upon heating and cooling through the phase transition (peak A in Fig. 2).

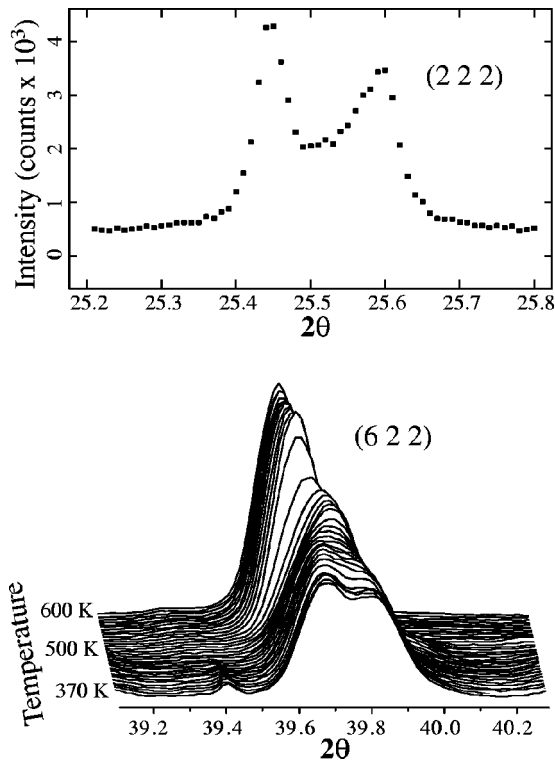


FIG. 4. Bragg reflections are seen to split in the low-temperature phase. The (222) peak shown is from the room-temperature X7A data ($\lambda=1.1628 \text{ \AA}$). The (622) peak shown is from the variable-temperature image plate XRD data ($\lambda=0.9341 \text{ \AA}$).

most if not all of the normal Bragg peaks are either split or anomalously broadened in the low-temperature phase, as shown in Fig. 4. The effect of the splitting on the width and shape of the peaks increases markedly with increasing 2θ , indicating a unit cell distortion. This distortion is sufficiently large that one cannot perform an acceptable Rietveld refinement without taking it into account. The most distinctly split normal Bragg peak in the low-temperature phase is the most intense peak in the pattern, the (222) peak near $2\theta=25.5^\circ$, which appears to be sliced into two nearly equal halves with a spacing of $\Delta(2\theta)=0.14^\circ$ or $\Delta d/d=0.0054$ (see Fig. 4). This splitting rules out tetragonal or orthorhombic distortions and specifically favors a monoclinic or rhombohedral angular distortion over a triclinic distortion that could split the peak into as many as four new peaks. The expected monoclinic and trigonal angular distortions can be shown to depend on the width of the cubic (hhh) peak splitting as follows: $\gamma_{\text{mono}}=\pi/2+\epsilon_{\text{mono}}$ and $\alpha_{\text{rhom}}=\pi/2+\epsilon_{\text{rhom}}$, respectively, where

$$\epsilon_{\text{mono}} \cong \frac{3}{2} \frac{\Delta d}{d} \quad \text{and} \quad \epsilon_{\text{rhom}} \cong \frac{3h}{8} \frac{\Delta d}{d}. \quad (1)$$

This yields $\epsilon_{\text{mono}}=0.0081$ (0.46°) and $\epsilon_{\text{rhom}}=0.0040$ (0.23°) for the observed (222) peak splitting. Using the Rietveld refinement facility of the GSAS software package,¹⁷ each of these two possibilities were examined via the Le Bail intensity extraction of the room-temperature X7A XRD data. The background, zero-error, peak-shape, and unit cell parameters were optimized in this way. The

TABLE I. Best Le Bail profile fits to room temperature synchrotron XRD data (beamline X7A) based on three types of cell distortion, rhombohedral, monoclinic, and triclinic.

$\alpha_{\text{rhom}}=9.1141 \text{ \AA}$	$\alpha_{\text{rhom}}=89.7843^\circ$	
$R_{\text{wp}}=10.39\%$	$R_p=8.09\%$	$\chi^2=1.503$
$a_{\text{mono}}=9.1131 \text{ \AA}$	$b_{\text{mono}}=9.1123 \text{ \AA}$	$c_{\text{mono}}=9.1396 \text{ \AA}$
$\alpha_{\text{mono}}=90^\circ$	$\beta_{\text{mono}}=90^\circ$	$\gamma_{\text{mono}}=90.4355^\circ$
$R_{\text{wp}}=8.95\%$	$R_p=7.20\%$	$\chi^2=1.111$
$a_{\text{tric}}=9.1130 \text{ \AA}$	$b_{\text{tric}}=9.1108 \text{ \AA}$	$c_{\text{tric}}=9.1392 \text{ \AA}$
$\alpha_{\text{tric}}=90.0031^\circ$	$\beta_{\text{tric}}=89.9793^\circ$	$\gamma_{\text{tric}}=90.4333^\circ$
$R_{\text{wp}}=8.93\%$	$R_p=7.16\%$	$\chi^2=1.107$

initial cell parameters were $a=b=c=9.1 \text{ \AA}$, $\gamma_{\text{mono}}=90.46^\circ$ in the first case and $a=9.1 \text{ \AA}$, $\alpha_{\text{rhom}}=90.23^\circ$ in the latter. And while a triclinic cell was also attempted, it resulted in cell parameters approximately equal to those of the monoclinic cell. It quickly became evident that both cells had merit, but the more complex monoclinic distortion handled the high-angle peak splittings better than the rhombohedral distortion. The results of these Le Bail fits are listed in Table I.

A revealing feature of the monoclinic fit is the approximate equivalence of the a and b lattice parameters. This a/b degeneracy is a clue to another subtle feature of the distorted cell, namely, that the observed monoclinic distortion of the 9 \AA cubic cell can be equivalently described as an orthorhombic distortion of a larger tetragonal cell related to the original cell by the transformation matrix $((1,1,0),(1,\bar{1},0),(0,0,1))$. This $\sqrt{2}a \times \sqrt{2}a \times a$ supercell (expressed hereafter as $\sqrt{2} \times \sqrt{2} \times 1$ for brevity) is rotated by 45° in the ab plane relative to the original cell and has twice the volume. The new orthorhombic cell parameters (a' , b' , and c') are geometrically related to the original monoclinic cell parameters ($a=b, c$, and $\gamma=\pi/2+\epsilon$) by the relations

$$\begin{aligned} a' &= \sqrt{2}a \sqrt{1-\sin(\epsilon)} \approx \sqrt{2}a(1-\epsilon/2), \\ b' &= \sqrt{2}a \sqrt{1+\sin(\epsilon)} \approx \sqrt{2}a(1+\epsilon/2), \\ c' &= c. \end{aligned} \quad (2)$$

An additional Le Bail profile refinement using the orthorhombic cell yielded the final room-temperature unit cell parameters shown in Table II, and the fits to several of the badly split peaks are shown in Fig. 5. An equivalent orthorhombic distortion parameter can also be defined as $\epsilon' \equiv 2(b'-a')/(b'+a')=0.0080$, which is easily shown to be equal to ϵ_{mono} . This supercell setting has been observed recently in anion-ordered $\text{Ca}_8[\text{Al}_{12}\text{O}_{24}](\text{MO}_4)_2$ sodalite.¹⁸

The fits to the background included a 15-segment reciprocal interpolation function (GSAS background function #8) added to a fixed 20-segment linear interpolation function.

TABLE II. Le Bail profile fit to the room temperature synchrotron XRD data (beamline X7A) based on the $\sqrt{2} \times \sqrt{2} \times 1$ pseudotetragonal supercell.

$a_{\text{orth}}/\sqrt{2}=9.1522 \text{ \AA}$	$b_{\text{orth}}/\sqrt{2}=9.0795 \text{ \AA}$	$c_{\text{orth}}=9.1372 \text{ \AA}$
$R_{\text{wp}}=8.59\%$	$R_p=7.03\%$	$\chi^2=1.023$

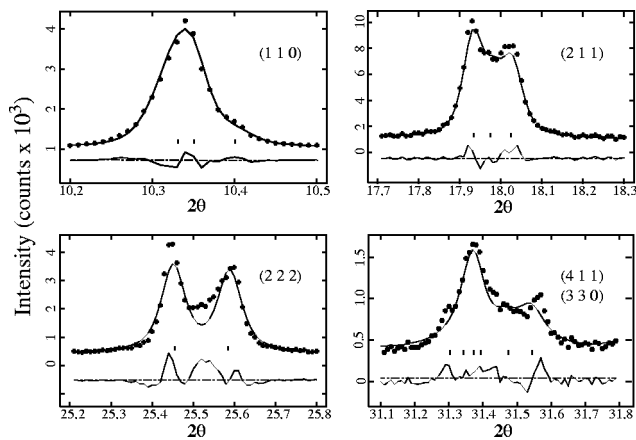


FIG. 5. Le Bail profile fits to several distorted Bragg peaks from the room-temperature X7A data ($\lambda=1.1628 \text{ \AA}$). The reflection markers correspond to the pseudo-tetragonal supercell, which was the cell used for the profile fit.

The zero error in each case was approximately 0.015° . The pseudo-Voigt profile shape of Thompson *et al.*¹⁹ was used, including the asymmetry correction of Finger *et al.*²⁰

C. Superlattice reflections

The pseudo-tetragonal $\sqrt{2}\times\sqrt{2}\times 1$ supercell upon which we indexed the Bragg reflection splittings has several advantages over any of the other cells tried. It has the highest symmetry, provides the best Le Bail fit to the normal Bragg reflections, and nicely explains all of the observed splittings. And very importantly, it predicts the positions of a number of observed superlattice peaks. Peaks A, C, E, I, J, and K of Fig. 2 index on the supercell as (101), (211), (301), (321), (410) or (302), and (411) or (103), respectively. In the original cubic setting, they are $(\frac{1}{2}21)$, $(\frac{3}{2}21)$, $(\frac{5}{2}21)$, $(\frac{7}{2}21)$, $(\frac{9}{2}21)$ or $(\frac{3}{2}22)$, and $(\frac{5}{2}21)$ or $(\frac{1}{2}23)$, respectively. This is encouraging evidence. The highest point-group symmetry possible for an orthorhombic cell is *mmm*, and the series of superlattice peaks that have sizeable intensities rule out systematic absences based on any centering symmetry. So while the structural complexity of the supercell has increased by at least a factor of 12 relative to the high-temperature structure, it is clear that the increase in the information content of the diffraction data is not anywhere near so great. Yet even if the whole body of superstructural detail cannot be extracted from the available data, some of the essential features can still be discerned with the aid of computer simulations as discussed below.

In addition to the superlattice peaks that were indexed on the $\sqrt{2}\times\sqrt{2}\times 1$ supercell, other superlattice peaks arose that this supercell could not explain. The largest of these is peak B in Fig. 2 between the ordinary (110) lattice peak, and the $(\frac{1}{2}21)$ superlattice peak. Peaks D, F, G, L, and M are also of this same class. As seen in the figure, these peaks also form at the phase transition near 500 K. Nothing about their temperature variation or profile shape distinguishes them from those already indexed on the $\sqrt{2}\times\sqrt{2}\times 1$ supercell, indicating that they result from the same ordering phenomenon. Two possibilities then need to be examined: (1) the existence of a larger supercell (i.e., a supercell of the $\sqrt{2}\times\sqrt{2}\times 1$ supercell),

and (2) an incommensurate modulation that forms in cooperation with the $\sqrt{2}\times\sqrt{2}\times 1$ supercell ordering.

The pattern is further complicated by a small number of extremely narrow peaks (FWHM $\sim 0.05^\circ$ as compared to 0.20° for the sodalite parent and satellite reflections) in the region $2\theta > 20^\circ$ which appear to be unrelated to the sodalite structure. Their intensities vary wildly but reversibly in the range from 365 K to 675 K and completely disappear somewhere between 365 K and 100 K. Furthermore these narrow peaks only appeared in the sample selected for this study which was cooled slowly after dehydration at high-temperature in order to obtain more pronounced superstructure. Other samples that were quenched quickly to room-temperature demonstrated the same superlattice peaks, but lacked these narrow peaks. Whatever their origin, the anomalously narrow widths of these peaks rendered them easy to differentiate and exclude in the analysis that follows. The small temperature-independent peak near $2\theta=15.3^\circ$ (peak H) is likely due to trace amounts of a condensed silicate impurity phase created during the hydroxysodalite synthesis.

D. A larger commensurate supercell?

In order to examine the possibility of a larger commensurate supercell, a method was sought for generating all possible reciprocal space superlattices, within reasonable limits, that might explain the additional superlattice peaks. Candidate superlattices were described in terms of the transformation matrix \mathbf{S} of integer elements whose row vectors represent the components of the new basis vectors, \mathbf{b}'_i , in terms of the old ones, \mathbf{b}_j , via the expression, $\mathbf{b}'_i = \sum_j \mathbf{S}_{ij} \mathbf{b}_j$. While this transformation matrix description is very useful, it is not unique, since any lattice can be described by an infinite number of bases. There are, however, algorithms for selecting one basis that uniquely identifies and distinguishes the underlying superlattice. The method of derivative lattices was used here and involves the selection of a lower-triangular matrix of integers that satisfies the following criteria:²¹

$$\mathbf{S} = \begin{pmatrix} p_1 & 0 & 0 \\ q_1 & p_2 & 0 \\ r_1 & q_2 & p_3 \end{pmatrix} \begin{cases} p_1 p_2 p_3 > 1 \\ -\frac{1}{2} p_1 < q_1 \leq \frac{1}{2} p_1 \\ -\frac{1}{2} p_1 < r_1 \leq \frac{1}{2} p_1 \\ -\frac{1}{2} p_2 < q_2 \leq \frac{1}{2} p_2 \end{cases} \quad (3)$$

There is guaranteed to be exactly one such integer matrix for each unique superlattice of a triclinic lattice with real-space cell volume ratio $V'/V = p_1 p_2 p_3$. For $V'/V = 2$, for example, there are seven unique superlattices that meet these requirements. If the symmetry is higher than monoclinic, even some of these bases may turn out to be equivalent due to the interchangeability of identical axes. In the case of a cubic lattice, the seven unique $V'/V = 2$ superlattices are reduced to three in number.

After generating a number of superlattices in this way, it was observed that cells with $V'/V > 8$ tended to produce such closely spaced arrays of superlattice peak positions that the observed superlattice peak positions could be assigned rather arbitrarily. Only cells with $V'/V \leq 8$ afforded a reasonable comparison against the XRD data. All such unique

supercells were generated and tested for the ability to yield the observed peak positions, and one candidate emerged from this analysis; a $3\sqrt{2}\times\sqrt{2}\times 1$ orthorhombic cell ($V'/V = 6$) obtained by tripling either the a or b -axis cell parameter of the $\sqrt{2}\times\sqrt{2}\times 1$ cell. This cell was also eventually discarded in favor of a long-period modulation for reasons that will be discussed below.

E. A modulated structure

In a one-dimensionally modulated structure, each Bragg reflection can be described in terms of the parent cell by a reciprocal space vector of the form $\mathbf{h} = (h\mathbf{a}^* + k\mathbf{b}^* + l\mathbf{c}^*) + m\boldsymbol{\tau}$, where h, k, l , and m are integers, and $\boldsymbol{\tau} = (\tau_a\mathbf{a}^* + \tau_b\mathbf{b}^* + \tau_c\mathbf{c}^*)$ with at least one of the τ_i being a noninteger. The direct-space modulation direction is then $(\tau_a^{-1}\mathbf{a} + \tau_b^{-1}\mathbf{b} + \tau_c^{-1}\mathbf{c})$, and $|\boldsymbol{\tau}|^{-1}$ is the period of the modulation. Structural modulations often tend to be smoothly sinusoidal in nature and yield satellite peak intensities that decrease sharply with increasing m , so that only first order satellites are important. And it is apparent from Fig. 2 that the clearly unindexed superlattice peaks are primarily clustered around the intense Bragg peaks of the cubic parent cell such as (110) and (310), as would be expected for low-order modulation-induced satellites.

The parameter space of possible modulation vectors in low-temperature $\text{Na}_6\text{-SOD}$ was searched using a modification of the method of Wilkinson *et al.*²² which was applied to the unindexed peak positions extracted from the 100 K image plate data. Only one-dimensional modulations were considered, they being the only cases that can be realistically addressed here. A figure of merit (FOM) was defined as a function of the modulation vector and monitored as the vector was systematically varied, the objective being to find the modulation vector that maximized the FOM. The principal deviations from the procedure of Wilkinson *et al.* were threefold: (1) Because the unindexed peaks were small and tended to cluster around the most intense Bragg peaks of the parent cell, satellites were only generated for these most intense peaks, (110), (112), (222), (310), and (400). (2) The FOM was defined as $\sqrt{(1/N)\sum_i^N w_i \Delta_i^2}$, where $\Delta_i = (|d_{\text{obs}} - d_{\text{calc}}|/d_{\text{obs}})_i$ and $w_i = \tan^2(\theta_{\text{obs}})_i$, the weighting factor accounting for the fact that the random errors in $2\theta_{\text{obs}}$ are expected to be constant across the pattern. (3) Both the magnitude and direction of the modulation vector were treated as unknowns and systematically varied.

Because the $\pm\boldsymbol{\tau}$ descriptions of the modulation direction are equivalent, it is only necessary to examine the FOM over modulation directions within the $+c$ hemisphere. Defining γ_a to be the angle between $\boldsymbol{\tau}$ and the orthorhombic $+a$ direction, and γ_b to be the angle between $\boldsymbol{\tau}$ and the $+b$ direction, $\gamma_x = (-\gamma_b - \gamma_a + 180^\circ)$ and $\gamma_y = (\gamma_b - \gamma_a)$, a grid search can be carried out in the convenient (γ_x, γ_y) coordinate system such that both angles range from 0° to 180° . Figure 6 is a contour plot of the FOM vs modulation direction over the entire $+c$ hemisphere using a ($\Delta_x = \Delta_y = 1.8^\circ$) grid at $|\boldsymbol{\tau}| = 0.2133 a_{\text{avg}}^{-1}$, where $a_{\text{avg}} = \frac{1}{3}(a/\sqrt{2} + b/\sqrt{2} + c) = 9.0706 \text{ \AA}$ at 100 K. γ_a and γ_b are the axes of the figure while γ_x and γ_y are the axes of the inner square. The maximum FOM values are indicated by the intense

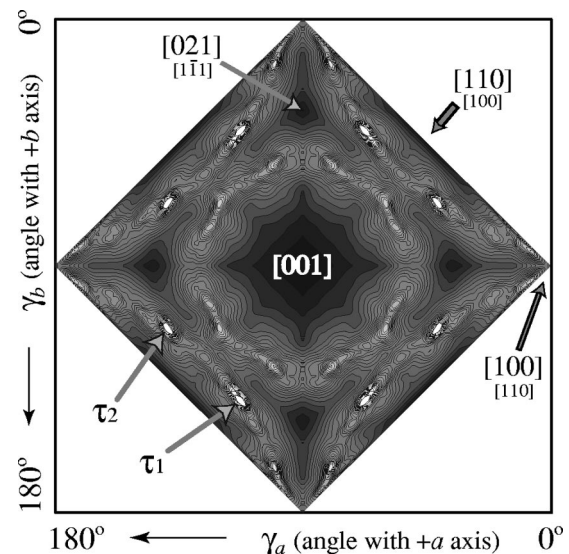


FIG. 6. Contour map (mesh size= 1.8°) of the figure-of-merit (FOM) vs modulation direction over the entire $+c$ hemisphere at $|\boldsymbol{\tau}| = 0.2133 a_{\text{avg}}^{-1}$. The FOM employs the distorted supercell parameters and the incommensurate peak positions from the 1 h 100 K image plate XRD data. White regions indicate a large FOM value. The FOM is slightly higher at τ_1 (630.3) than at τ_2 (621.6). In the supercell setting, τ_1 corresponds to $(\bar{1} \bar{2} 1)/8.9$ and τ_2 to $(\bar{2} \bar{1} 1)/8.9$, both of which are parallel to reciprocal lattice vectors of the supercell.

white spots in the figure, and several of the principal directions are labeled according to both the orthorhombic supercell setting (larger font) and the original cubic setting (smaller font). The modulation direction at the maximum is ($\gamma_a = 67.5^\circ, \gamma_b = 40.5^\circ$) and yields a final modulation vector of $(0.2133 a_{\text{avg}}^{-1})(0.3827 \ 0.7604 \ 0.5247)$, which is $(2.034 \ 1.032 \ 1.000)/8.913 \cong (211)/8.9$ in reciprocal lattice units in the supercell setting, or $(\frac{3}{2} \frac{1}{2} 1)/8.9$ in the original cubic setting. The modulation period was determined by constructing similar plots using values of $|\boldsymbol{\tau}|$ in the range from 0 to $0.5 a_{\text{avg}}^{-1}$ at $0.002 a_{\text{avg}}^{-1}$ intervals and a grid size of $\Delta_x = \Delta_y = 6^\circ$. The peak near ($\gamma_a = 67.5^\circ, \gamma_b = 40.5^\circ$) was much stronger than any others observed and displayed a sharp maximum at $0.2133 a_{\text{avg}}^{-1}$ indicating an unambiguous best solution.

Because the FOM was calculated in the supercell setting using the orthorhombically distorted cell parameters, it has an obvious pseudotetragonal symmetry in Fig. 6. There appear to be eight equivalent modulation directions, though there are actually two sets of four, τ_1 being slightly favored over τ_2 . A remnant of the broken threefold cubic symmetry is also evident near the $\langle 111 \rangle$ directions of the cubic parent cell. Of the original 24 equivalent $\langle \frac{3}{2} \frac{1}{2} 1 \rangle$ directions, those that best reproduce the satellite peak positions (i.e., have high FOM values) are precisely those eight that are parallel to reciprocal lattice vectors associated with the new $\sqrt{2}\times\sqrt{2}\times 1$ supercell, suggesting that the supercell ordering and long-period modulation occur cooperatively. The observed and calculated positions of these peaks, along with the indices of the parent Bragg reflections to which they are $m = +1$ satellites, are listed in Table III.

Modulated structures have also been reported for sodalite as well as for other host-guest materials. Depmeier

TABLE III. Observed and calculated $m=+1$ incommensurate satellite peaks.

(hkl) supercell	(hkl) parent cell	$2\theta_{\text{calc}}(^{\circ})$	$2\theta_{\text{obs}}(^{\circ})$	$2\theta_{\text{diff}}(^{\circ})$
$(1\ 1\ \bar{1})$	$(0\ 1\ \bar{1})$	7.65	7.67	0.02
$(\bar{2}\ 0\ \bar{2})$	$(\bar{1}\ \bar{1}\ \bar{2})$	13.60	13.63	0.03
$(3\ \bar{1}\ \bar{1})$	$(1\ \bar{2}\ \bar{1})$	14.04	14.04	0.00
$(3\ \bar{1}\ \bar{1})$	$(2\ 1\ \bar{1})$	14.87	14.88	0.01
$(\bar{3}\ \bar{3}\ \bar{1})$	$(\bar{3}\ 0\ \bar{1})$	17.51	17.46	-0.05
$(1\ \bar{1}\ \bar{3})$	$(1\ 0\ \bar{3})$	18.38	18.35	0.03
$(\bar{1}\ 1\ 3)$	$(\bar{1}\ 0\ 3)$	18.99	19.02	0.03
$(0\ 4\ \bar{2})$	$(\bar{2}\ 2\ \bar{2})$	19.37	19.38	0.01
$(4\ 4\ 0)$	$(4\ 0\ 0)$	22.71	22.75	0.04
$(0\ 0\ 4)$	$(0\ 0\ 4)$	23.01	23.03	0.02

performed a number of studies on the tungstate and molybdate aluminate sodalites that reveal modulated low-temperature phases involving periodic distortions or tilts of the framework tetrahedra.^{13,23,24} An approximately commensurate modulation with $\tau \approx 0.2a^*$ due to EF cation ordering was reported by Schlenke *et al.*²⁵ in a single crystal x-ray diffraction study of the dehydrated Na form of zeolite morденite. Incommensurately modulated guest lattices have been found in Li-intercalated $\text{Li}_x\text{V}_2\text{O}_5$ bronzes,²⁶ and also proposed to explain fine-structure in the NMR spectra of acetone intercalated graphite, Li-intercalated transition metal chalcogenides, and zeolite Tl-natrolite.²⁷

IV. RESULTS AND DISCUSSION: SUPERSTRUCTURE ANALYSIS

A. Symmetry considerations

The maximum topological space-group symmetry of the sodalite framework²⁸ is $Im\bar{3}m$, corresponding to an ideal SiO_2 framework with no Pauling tilt or other distortion—one T-atom on the Wyckoff $c(\frac{1}{4}, \frac{1}{2}, 0)$ position with multiplicity 12 and one oxygen on the Wyckoff $c(x \sim 0.33, x, 0)$ position with multiplicity 24. The Pauling tilt of the TO_4 tetrahedra preserves body-centering symmetry, but reduces the point symmetry from octahedral to tetrahedral, resulting in space group $I\bar{4}3m$. In this case, each cation shifts to one side of its window or the other, in such a way as to place four cations per sodalite cage in a tetrahedral arrangement relative to the cage center, the orientation of the tetrahedron being the same in every cage.¹ Differentiating between Al and Si sites in a 1:1 ordered alumino-silicate framework, on the other hand, preserves the octahedral point symmetry, but destroys the body centering, leading to space group $Pm\bar{3}n$. Si/Al ordering and Pauling tilt can also be considered simultaneously, in which case the highest possible symmetry is $P\bar{4}3n$, which is a maximal subgroup of both $I\bar{4}3m$ and $Pm\bar{3}n$.¹³

For sodalite structures with tetrahedral anions and/or complete tetrahedral cation configurations in each cage, $I\bar{4}3m$ and $P\bar{4}3n$ would be natural reference points from which to begin investigating distortions to lower-symmetry configurations. For Na_6 -SOD, however, some cation sites are vacant, and the restriction of examining only subgroups of tetrahedral point symmetry may not be valid. For this reason, $Pm\bar{3}n$ will be the reference point for further analysis,

which only assumes the ordering of the Si and Al over the framework T-sites. In an untilted $Pm\bar{3}n$ sodalite framework, assuming the origin to be at the center of the sodalite cage, the T-atoms sit at the Wyckoff $c(\frac{1}{4}, \frac{1}{2}, 0)$ and $d(\frac{1}{4}, 0, \frac{1}{2})$ positions with multiplicities of 6, the oxygen sits at the Wyckoff $k(x \sim 0.33, y \sim x, 0)$ position with a multiplicity of 24 ($x \neq y$ because Al-O and Si-O bond lengths differ), and the window-center sodium is positioned at the Wyckoff $e(\frac{1}{4}, \frac{1}{4}, \frac{1}{4})$ position with multiplicity 8. The Pauling tilt is characterized by a shift of the oxygen z parameter to a nonzero value, in which case the tilt angle is $\varphi = \tan^{-1}[z/(0.5-x)]$.

B. Enumeration and classification of possible cation configurations

The low-temperature cation ordering responsible for the $\sqrt{2} \times \sqrt{2} \times 1$ supercell reported here for Na_6 -SOD can only be configured in a limited number of ways. Each Na^+ cation occupies a site near the center of one of the 6-ring windows that join adjacent sodalite cages, and each original 9 Å unit cell contains eight of these 6-ring windows. The set of all such sites throughout the crystal form a primitive cubic lattice with edge length equal to $a/2$. This lattice will be referred to as the cation lattice (CL) throughout the remainder of this discussion. Because $\frac{1}{4}$ of the CL sites are vacant, the problem of enumerating the possible cation configurations then reduces to the problem of distributing vacancies on the CL.

For orderings that are restricted to the 9 Å cubic unit cell, one simply needs to consider the number of different ways to distribute the 6 cations (or two vacancies) over the 8 available sites. This number is 28, which then reduces by symmetry to 3 unique arrangements in which the two vacancies are either separated by an edge, face-diagonal, or body-diagonal vector of the CL. The possibility that cations may shift off from the window-center position is unimportant here. Small off-window shifts are a “fine” detail compared to the “coarser” effect of having some window sites occupied and others unoccupied. The challenging problem of examining the “off-window” cation configurations was undertaken as well, but did not prove worthwhile.

In the $\sqrt{2} \times \sqrt{2} \times 1$ supercell, there are 16 6-ring window sites and 12 cations to fill them. The total number of vacancy distributions over these sites is then $\binom{16}{12} = 1820$. It proved useful for purposes of unambiguous definition to label the 1820 configurations with the algorithm used to generate them. A stack of nested DO loops was executed in which \mathbf{i} was incremented from 4 to 16, \mathbf{j} from 3 to $\mathbf{i}-1$, \mathbf{k} from 2 to $\mathbf{j}-1$, and \mathbf{l} from 1 to $\mathbf{k}-1$, so as to count from 1 to 1820. Each set of $(\mathbf{i}, \mathbf{j}, \mathbf{k}, \mathbf{l})$ traversed by the loop corresponds to vacancy placement on the \mathbf{i} th, \mathbf{j} th, \mathbf{k} th, and \mathbf{l} th cation sites, which were numbered from 1 to 16 in the following order: $\{(0, \frac{1}{4}, \frac{1}{4}), (\frac{1}{2}, -\frac{1}{4}, \frac{1}{4}), (0, -\frac{1}{4}, \frac{1}{4}), (\frac{1}{2}, \frac{1}{4}, \frac{1}{4}), (0, \frac{1}{4}, -\frac{1}{4}), (\frac{1}{2}, -\frac{1}{4}, -\frac{1}{4}), (0, -\frac{1}{4}, -\frac{1}{4}), (\frac{1}{2}, \frac{1}{4}, -\frac{1}{4}), (\frac{1}{4}, 0, \frac{1}{4}), (-\frac{1}{4}, \frac{1}{2}, \frac{1}{4}), (-\frac{1}{4}, 0, \frac{1}{4}), (\frac{1}{4}, \frac{1}{2}, \frac{1}{4}), (\frac{1}{4}, 0, -\frac{1}{4}), (-\frac{1}{4}, \frac{1}{2}, -\frac{1}{4}), (-\frac{1}{4}, 0, -\frac{1}{4}), (\frac{1}{4}, \frac{1}{2}, -\frac{1}{4})\}$. The index or identification number of each configuration is its order in the DO loop stack, from 1 to 1820.

Because many of these configurations are related by symmetry, the number of unique configurations is consider-

TABLE IV. 88 unique cation orderings of Na₆-SOD in the $\sqrt{2}\times\sqrt{2}\times 1$ supercell setting.

Triclinic (S.G. symmetry ^a =1; deg=32)														
	71	75	76	77	78	79	80	87	89	97	98	101	102	105
$C_{\#}$	72	81	85	84	83	82	86	88	90	99	100	113	103	120
	189	190	191	192	273	274	275	276	559	560	589	625		
Monoclinic (Deg.=4 for C_{15} , 8 for $C_{624}-C_{673}$, and 16 for the others)														
$C_{\#}$	2	3	4	5	11	12	15 ^b	22	184	185	202			
S.G.	3	3	3	3	3	3	...	3	4	3	4			
$C_{\#}$	203	269	287	301	302	303	304	561	588 ^c	624 ^d	670 ^d			
S.G.	3	3	3	3	3	3	3	7	...	12	12			
Orthorhombic							Tetrag.							
$C_{\#}$	1 ^b	10 ^b	21	24	28	29	183 ^b	197 ^b	268 ^d	286 ^d	558 ^d	587 ^d	315	297
S.G.	21	40	53	52	49	48	40	21	35	21	38	39	93	111
Deg.	4	4	4	4	4	4	8	8	8	8	8	8	4	4

^aSpace groups are numbered as in current editions of the *International Tables of Crystallography*, Vol. A.

^bThese cells are primitive in the parent $1\times 1\times 1$ cell, which is also the conventional cell for C_{15} ($R\bar{3}c$).

^cThe conventional cell (Pc) has $a=a_0$, $b=\sqrt{2}a_0$, $c=\sqrt{3}a_0$, $\alpha=\gamma=90^\circ$, $\cos(\beta)=1/\sqrt{3}$, and $V'/V=2$.

^dThe conventional cell is a C -centered supercell with $a=b=2a_0$, $c=a_0$, $\alpha=\beta=\gamma=90^\circ$, and $V'/V=4$. The space-group symmetry indicated refers to this setting.

ably less than 1820. Each unique configuration can be represented by any of its symmetry equivalent configurations. So for a given unique configuration, the set of its symmetry equivalents will be referred to here as an ‘‘equiset,’’ and simple group-theoretical considerations lead to the conclusion that the number of distinct members of an equiset must be a divisor of the total number of applied symmetries. A total of 4 symmetries, for example, allows for equisets with 1, 2, or 4 members or elements. In the original cubic cell, the task of determining the number of equisets was trivial (recall that there were 3), whereas in the supercell the situation becomes a little more complicated. The uniqueness of a configuration depends not only on the arrangement of the cations with respect to one another, but on their relationship to the framework atoms. Two configurations that are equivalent relative to a rather high framework symmetry may no longer be equivalent if the framework symmetry is lowered. So the uniqueness of a cation configuration is actually defined relative to the symmetry of the framework within the setting of the supercell. This ideal $Pm\bar{3}n$ symmetry can be considered as a starting point for subsequent distortions that will further split these ‘‘parent’’ equisets into smaller ones during the structural energy minimization discussed below.

The reduction from $Pm\bar{3}n$ symmetry to the appropriate highest-possible framework symmetry in the $\sqrt{2}\times\sqrt{2}\times 1$ supercell setting can then be considered in two steps. First, $Pm\bar{3}n$ must reduce to $P4_2/mmc$ within the original cell in order to eliminate the threefold axes. This reduces the number of symmetries in the original unit cell (i.e., the multiplicity of the general Wyckoff position) by a factor of 3, from 48 to 16. Secondly, the 45° transformation to the $V'/V=2$ supercell basis doubles the number of symmetries to 32. These 32 symmetries were then applied to each of the 1820 cation configurations, and configurations that proved to be symmetry equivalent were grouped together into equisets. Of the

original 1820 configurations, only 88 proved to be unique. In choosing a convenient and unambiguous identification label for each equiset, the decision was made not to simply number them from 1 to 88. Instead, each of these 88 equisets was labeled according to the index of its element of lowest index. For instance, a 16-element equiset in which configuration 5 was the element of lowest index was called ‘‘unique configuration 5,’’ or simply ‘‘ C_5 .’’ Each equiset is listed in Table IV together with its degeneracy (i.e., the number of elements in the equiset) and space-group symmetry. The conventional unit cell and space-group symmetry of each unique configuration was determined using the FindSymmetry facility of MSI’s InsightII software suite.²⁹

The space-groups listed in Table IV generally indicate more symmetry than will be possessed by the actual distortion driven by a given configuration because the parent framework symmetry used ($Pm\bar{3}n$) does not activate degrees of freedom such as the Pauling tilt, etc. If a Pauling tilt is assumed by lowering the parent framework symmetry to $P\bar{4}3n$, many of these 88 equisets become further divided, and the new space-group symmetries are easily deduced from those listed. If the parent framework symmetry is raised to $Im\bar{3}m$, there are only 62 equisets instead of 88. Pairs of equisets that were originally joined together in this higher symmetry are paired together in the same entry in Table IV.

C_1 and C_{197} can actually be considered as identical for our purposes. C_1 and C_{197} are distinct relative to the ideal tetragonal symmetries of the $\sqrt{2}\times\sqrt{2}\times 1$ supercell, but are related by a threefold axis of the original cubic cell. Thus, they are only superficially distinct relative to the periodic boundary conditions employed in a computer simulation of the supercell contents. They drive identical physical distortions since nature imposes no artificial constraint on the orientation of the supercell. The only other configurations with such a relationship are C_{10} and C_{183} . These four cells are

base centered and have the $1\times 1\times 1$ parent cell as their primitive unit cell. In fact, (C_1, C_{197}) , (C_{10}, C_{183}) and C_{15} are precisely the three unique vacancy configurations associated with the $1\times 1\times 1$ parent cell.

C. Configurational energetics

Now that the cations orderings of the $\sqrt{2}\times\sqrt{2}\times 1$ supercell have been enumerated and turn out to be manageably few in number, it is desirable to determine which ordering is actually responsible for the low-temperature supercell formation. If single crystal diffraction data could be obtained, and a sufficient number of intense superlattice peaks measured, the problem could probably be solved by traditional crystallographic methods. But the limited information content of the powder diffraction data available makes it necessary to rely upon computer modeling to guide the search. Shannon *et al.*¹⁵ have determined the structural energies of these 88 unique cation configurations by means of lattice energy minimizations employing an empirical force-field (the BMW potential³⁰) specifically tailored for sodalite calculations. This allowed them to rank the cation orderings according to their relative energies and to examine the lowest-energy configurations in more detail by means of *ab initio* GGA density functional calculations using both hard and soft pseudopotentials.

We point out here that their five lowest-energy configurations prior to energy minimization (C_1 , C_5 , C_{15} , C_{24} , and C_{29}) are closely related in a variety of ways. They do not, for example, allow nearest-neighbor vacancies (NNV's), which are vacancy pairs separated by a CL edge vector. NNV's are energetically undesirable because they fail to minimize the inter-cation Coulomb repulsion by spreading the cation charges as evenly as possible throughout the crystal. We count a total of 10 NNV-avoiding configurations, the other five of which have higher energies for other reasons. Each of these five low-energy vacancy orderings also adheres to the general scheme illustrated in the upper left corner of Fig. 7, in which half of the [001] columns of cation sites contain no vacancies at all (indicated by solid circles) while the other half contain vacancies at every other position (indicated by empty circles). For the columns with vacancies, there is another degree of freedom; vacancy placement at $z = +\frac{1}{4}$ (distinguished by a “+”) vs placement at $z = -\frac{1}{4}$ (distinguished by a “-”). Because four vacancy-containing columns intersect the supercell, the five unique ways (taking the framework symmetry into account) to assign the $z = \pm\frac{1}{4}$ columns are precisely these five low-energy configurations. After energy minimization, Shannon *et al.*¹⁵ report that C_{286} , which is also one of the NNV-avoiding configurations, becomes the overall third-lowest energy configuration, thus joining these other five structures at the bottom of the energy scale.

Figure 8 contains a comparison between the observed 100 K image plate data and the calculated powder diffraction patterns of the C_1 , C_5 , C_{15} , C_{24} , C_{29} , and C_{286} models using coordinates from the DFT calculations of Shannon *et al.* Peaks associated with markers in one or both of the bottom two rows are associated with the original cubic cell, while peaks associated with markers from only the top two rows are superlattice peaks. Because deviations from body-

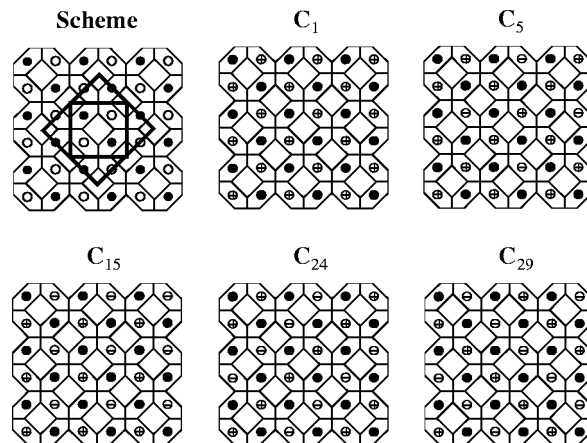


FIG. 7. The lowest-energy cation-orderings of the $\sqrt{2}\times\sqrt{2}\times 1$ supercell. Solid lines are an idealized [001] projection of the sodalite framework and circles represent the [001] columns of cation sites that comprise the CL. The diagram in the upper-left corner reveals the distribution of vacancy-containing columns intrinsic to the whole family of lowest-energy configurations, the two concentric squares representing the original cubic cell and the supercell. Solid circles are columns with no vacancies and empty circles are columns that contain vacancies at every other site. The remaining diagrams are the five specific instances of this general scheme. Circles containing a “+” or a “-” represent columns in which the vacancies are located at $z = +\frac{1}{4}$ or $z = -\frac{1}{4}$, respectively.

centering, due mainly to the strict ordering of Si and Al over the framework T-sites, are relatively small, even in the high-temperature parent structure, the ordinary $h+k+l=2n+1$ peaks also have intensities comparable to those of the superlattice peaks. It is not surprising to find discrepancies between the observed powder diffraction pattern and each of the calculated patterns since no attempt has been made here to model the long-period modulation. Modulation satellite peaks and changes to the commensurate peak intensities in-

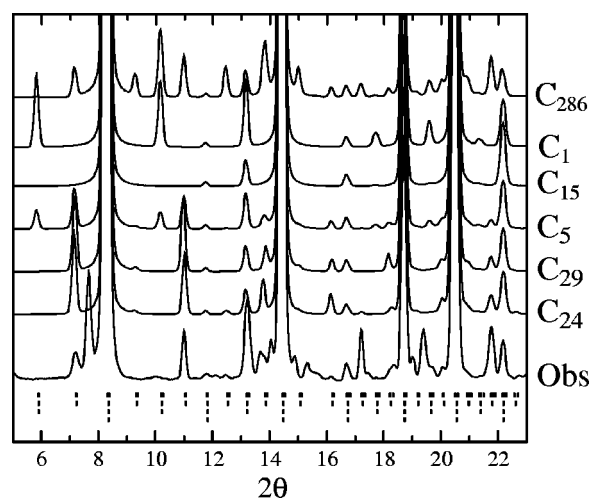


FIG. 8. Comparison of the experimental 100 K image plate XRD data and the calculated powder diffraction patterns of the five low-energy configurations. The four rows of reflection markers represent the following cells from top to bottom, respectively: (1) the distorted $\sqrt{2}\times\sqrt{2}\times 1$ supercell: $a = 12.8645 \text{ \AA}$, $b = 12.7621 \text{ \AA}$, $c = 9.0912 \text{ \AA}$ (define $a_{\text{avg}} = \frac{1}{3}(a/\sqrt{2} + b/\sqrt{2} + c) = 9.0706 \text{ \AA}$); (2) the undistorted $\sqrt{2}\times\sqrt{2}\times 1$ supercell: $a/\sqrt{2} = b/\sqrt{2} = c = a_{\text{avg}}$; (3) the original cubic cell: $a = a_{\text{avg}}$; and (4) the original cubic cell taking into account the systematic absences due to body-centering.

duced by the modulation have not been simulated. Only a detailed model of the modulation and a full refinement of both the commensurate superstructure and the modulation will produce a good fit to the entire pattern. The comparison in Fig. 8 is only qualitative. The point to examine carefully in each calculated pattern is the presence or lack of the correct commensurate satellite peaks.

C_{15} best maximizes the average inter-vacancy separation by strictly alternating it $z = \pm \frac{1}{4}$ columns in both the a and b directions (supercell setting) and therefore minimizes the $\text{Na}^+ - \text{Na}^+$ Coulomb repulsion energy. One can imagine constructing this configuration by starting without any window vacancies and then removing the same two cations from every unit cell along the $[111]$ diagonal, resulting in a rhombohedrally distorted ($\epsilon_{\text{DFT}} = -0.3247^\circ$) version of the original unit cell. The principal problems with C_{15} are that it cannot explain the orthorhombic distortion or produce superlattice peaks. While C_1 has the advantage of driving an orthorhombic distortion, it appears to have the least desirable inter-vacancy separation since there is no alternation between $z = \pm \frac{1}{4}$ columns, making it the highest energy configuration of the family. Furthermore, though its symmetry is best described as a base-centered configuration in the supercell setting, C_1 's primitive unit cell is simply the original cubic cell, so that like C_{15} , it also fails to yield superlattice peaks. C_5 is somewhat of an improvement—it has limited $z = \pm \frac{1}{4}$ vacancy alternation and results in a series of superlattice peaks—but the monoclinic distortion that it drives ($\epsilon_{\text{DFT}} = -0.18^\circ$) results in a number of significant superlattice peaks that are not observed.

C_{24} and C_{29} , with $z = \pm \frac{1}{4}$ vacancy alternation in one direction (either a or b), are the only two configurations in the lowest-energy family that drive an orthorhombic supercell distortion and lead to systematic absences among the superlattice peaks that are consistent with the observed powder diffraction pattern. If the framework is ignored, the vacancy arrangements of C_{24} and C_{29} on the CL are identical. In fact, they only differ in their orientations relative to the framework. As a result, their calculated XRD patterns are very similar and their unminimized Coulomb repulsion energies are identical. However, the force-field and DFT calculations of Shannon *et al.* reveal that their distinct orientations relative to the framework result in substantially different framework responses. After minimization C_{29} ends up between C_1 and C_5 in energy, while C_{24} drops below C_{15} to the very bottom of the list by a substantial margin.

C_{24} then emerges as the best solution for the low-temperature ordering of dehydrated salt-free sodium sodalite, having the following merits: (1) It belongs to the low-energy family of NNV-avoiding configurations in Fig. 7. (2) It is the overall lowest-energy solution by a significant margin, according to both DFT and BMW force-field calculations. (3) The configuration is inherently orthorhombic (being only one of 8 such orderings). The distortion that C_{24} drives in the DFT calculations¹⁵ ($a = 12.9723 \text{ \AA}$, $b = 12.9115 \text{ \AA}$, $c = 9.1719 \text{ \AA}$) provides the best qualitative fit to the observed distortion (see Table II); $\epsilon_{\text{obs}} = 0.0076$ vs $\epsilon_{\text{DFT}} = 0.0047$, and $\zeta_{\text{obs}} = 0.79$ vs $\zeta_{\text{DFT}} = 0.98$, where $\epsilon = 2(a-b)/(a+b)$ and $\zeta = (\sqrt{2}c-b)/(a-b)$. (4) It is one of only two configurations

(the other being C_{29}) that yields systematic absences among the superlattice peaks consistent with the observed powder diffraction pattern. The vacant windows of C_{24} are located at $(\frac{1}{2}, \frac{1}{4}, \frac{1}{4})$, $(\frac{1}{2}, -\frac{1}{4}, \frac{1}{4})$, $(0, \frac{1}{4}, -\frac{1}{4})$, and $(0, -\frac{1}{4}, -\frac{1}{4})$.

D. Larger commensurate supercell vs incommensurate modulation

The effort to use a larger commensurate supercell ($V'/V \leq 8$) to explain the superlattice peaks that were not indexed by the smaller $\sqrt{2} \times \sqrt{2} \times 1$ supercell did lead to one possibility: the $3\sqrt{2} \times \sqrt{2} \times 1$ supercell with $V'/V = 6$. The information gained from the calculated energies of the cation orderings in the $\sqrt{2} \times \sqrt{2} \times 1$ supercell were then brought to bear on potential orderings in this larger supercell. Candidate orderings were also required to (1) have orthorhombic point symmetry in order to be compatible with the observed peak splittings, (2) be primitive, so as not be equivalent to any smaller cell, and (3) avoid NNV's. Powder diffraction patterns were deduced for each of the unique configurations that satisfied these requirements, but none produced an array of superlattice peaks that resembled the experimental XRD data. Thus no commensurate $V'/V \leq 8$ supercells were found that explain all the observed superlattice peaks. The $\tau = (\frac{3}{2}1)/8.9$ modulation, on the other hand, accounts well for the peaks that are not associated with the $\sqrt{2} \times \sqrt{2} \times 1$ supercell, and its direction is parallel to the most intense commensurate superlattice reflection of the $\sqrt{2} \times \sqrt{2} \times 1$ supercell.

E. Rietveld analysis of the low-temperature cation-ordered phase

A Rietveld refinement of the C_{24} model of $\text{Na}_6\text{-SOD}$ was performed using a slice of the variable-temperature image plate data prepared by integrating over 50 pixels (i.e., an average over a temperature range 11.7 K wide) along the temperature axis centered at 393 K, which is still well below the ordering transition. The room-temperature X7A data had higher resolution, but was only a quick scan intended for examining the splitting of the principal peaks in the pattern. Because the (110) peak was saturated, it was excluded from the refinement. The narrow regions surrounding each of the extremely narrow peaks described in Sec. III C were also excluded. The background and profile shape were handled in a manner similar to that described for the fits in Table I. The results of the 393 K refinement are shown in Fig. 9. The largest difference peaks in Fig. 9 arise from the fact that the angular variation of the profile shape obtained when using an image plate requires special treatment¹⁶ that is not yet available in the GSAS¹⁷ software suite. Discrepancies associated with the effect of the long-period modulation (as discussed above) are also evident, but the match to the commensurate satellite peaks is considerably improved. A similar refinement of the 1 h 100 K image plate data was also carried out.

According to Table IV, the unrelaxed C_{24} configuration has space-group symmetry $Pnna$. Because the DFT calculations of Shannon *et al.* yielded Pauling tilt angles on the order of $13^\circ - 16^\circ$ for each of the low-energy cation configurations, it is important to note that a nonzero tilt angle reduces the symmetry of C_{24} to from $Pnna$ to $Pnc2$. In low-

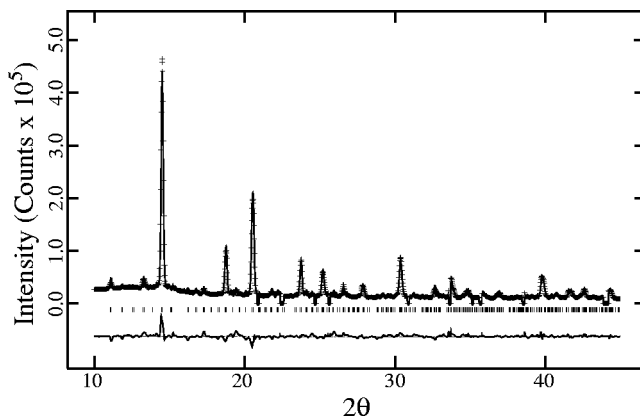


FIG. 9. Rietveld refinement (constrained-tetrahedra) of the structure of $\text{Na}_6\text{-SOD}$ at 393 K in the C_{24} cation configuration using the variable-temperature image plate XRD data. There were 74 refined parameters including the scale factor, zero error, 3 cell parameters, 3 isotropic thermal parameters, 63 positional parameters, and 4 profile parameters.

er the symmetry from $P\bar{4}3n$ in the parent cell to $Pnc2$ in the supercell setting, the number of free positional parameters goes from 4 to 63. Because the increase in the information content of the XRD data associated with the formation of the superlattice peaks was small compared to the increase in structural complexity, restraints had to be imposed to obtain convergence. The shape of the TO_4 tetrahedra were fixed by restraining both the T–O bond lengths and the O–O distances along the edges of each tetrahedron. Si–O and Al–O bond lengths were fixed at 1.61 Å and 1.74 Å, respectively, and O–O distances at $\sqrt{(8/3)} \times (\text{T–O}) = 2.63$ Å and 2.84 Å, respectively. The weight of the restraints was set high (weight = 10^7 , $\sigma = 0.01$ Å), effectively turning them into constraints, because loosening the weights of the restraints caused large random variations in the bond lengths and increases in the R -factor. We note that in order to obtain convergence, it was also necessary to damp the Na positional parameters, finally removing the damping factors only in the final refinement cycles.

The 393 K unit cell and profile parameters were refined together with the model, and the final weighted R -factor was 10.57%. The cell parameters, $a = 12.9481(16)$, $b = 12.8745(16)$, $c = 9.1569(16)$, were similar to those obtained from the Le Bail profile fits to the room-temperature X7A data in Table II. The resulting Pauling tilt angles refined to be to $\varphi_{\text{Si}} = 10.3^\circ$ and $\varphi_{\text{Al}} = 9.6^\circ$ (unit cell averages). Compare these values to those obtained from the DFT calculations of Shannon *et al.* ($\varphi_{\text{Si,DFT}} = 15.4^\circ$, $\varphi_{\text{Al,DFT}} = 14.5^\circ$) and those obtained from the similar 100 K refinement ($\varphi_{\text{Si}} = 14.4^\circ$, $\varphi_{\text{Al}} = 13.5^\circ$). Figure 10 illustrates the similar Pauling tilt angles obtained from the DFT calculation and the 100 K refinement.

Na(1) and Na(3) both refined nicely near the centers of their respective windows. The Na(1)–O distances were 2.33(7), 2.45(7), and 2.48(7) Å to the inner bonded oxygens, as well as 2.91(7), 2.85(4), and 2.79(7) Å to the outer non-bonded oxygens. The Na(3)–O_{inner} distances were 2.31(4), 2.29(4), and 2.20(4) Å, while the Na(3)–O_{outer} distances were 3.10(4) Å, 3.00(4) Å, and 2.89(4) Å. The oxygen environment at Na(2), however, was somewhat more interesting.

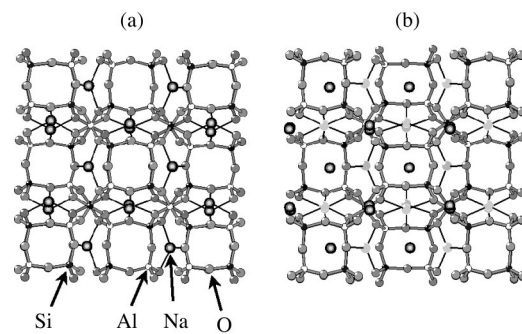


FIG. 10. The structure of $\text{Na}_6\text{-SOD}$ in cation configuration C_{24} from (a) the DFT calculations of Shannon *et al.* and (b) from the 100 K Rietveld refinement.

The TO_4 tetrahedra that form the vacant windows in each sodalite cage are still forced to undergo a Pauling tilt because they must cooperate in properly coordinating the cations of neighboring windows. But at 393 K, the vacant windows are considerably expanded (i.e., untilted) relative to the others, looking more like regular hexagons than clover leaves when viewed down the pseudo-3-fold axis. This local untilting especially seemed to effect Na(2), which refined to a position closer to the edge than the center of its window, where it coordinated to only two oxygens at distances of 2.38(4) and 2.15(4) Å. Even when the Na(2)–O distances were restrained so as to keep Na(2) coordinated to all three inner oxygens of the 6-ring, the best Na–O distances that could be obtained at 393 K were 2.38(4), 2.57(4), and 2.57(4) Å, which are still uncomfortably long. This is in contrast to the 100 K refinement where it was possible to obtain four reasonable Na(2)–O distances (restrained) of about 2.3 Å.

It is possible that the inability to include the long-period modulation in the refinement could lead to an “apparent” increase in the Na–O distances below the phase transition. It was recently demonstrated,³¹ for example, in the case of a modulated high- T_c superconducting cuprate structure, that including the modulation in the refinement significantly improved the Cu–O distances, which otherwise appeared to be uncharacteristically long when the modulation was ignored. However, a loss of adequate cation coordination environments with increasing temperature was observed by Behrens *et al.*³² in $\text{Ag}_6\text{-SOD}$ [$\text{Ag}_6\text{-SOD}$]. They reported a structural transition from a low-temperature cubic phase with static cation disorder to a high-temperature phase characterized by dynamic cation disorder as well as framework disorder amongst equal and opposite Pauling tilt angles ($\pm\varphi$) of the TO_4 tetrahedra. As the transition temperature was approached from below, the observed Pauling tilt angles grew small ($\varphi_{\text{Si}} = 8.3^\circ$, $\varphi_{\text{Al}} = 7.3^\circ$), the Ag–O_{inner} bond lengths grew uncomfortably long (2.50 Å), and the cell volume expanded as a result of the untilting, much like the results of the present refinements of the C_{24} model of cation-ordered $\text{Na}_6\text{-SOD}$.

F. Rietveld analysis of the high-temperature cation-disordered phase

Felsche *et al.*⁵ applied $P\bar{4}3n$ symmetry to the structural model of the cubic high-temperature $\text{Na}_6\text{-SOD}$ in their best

TABLE V. Structural parameters from the 675 K cubic phase (bond lengths in Å).

Atoms	X	Y	Z	Occupancy	U_{iso} (Å ²)
Ordered-tilt model refinement ($P\bar{4}3n$)					
Si	0.25	0.5	0	1	0.032(3)
Al	0.25	0	0.5	1	0.039(3)
O	0.1463(5)	0.1553(5)	0.4927(10)	1	0.052(1)
Na	0.2351(5)	0.2351(5)	0.2351(5)	0.75	0.052(2)
4×Si–O	1.599(5)	4×O–Si–O	107.13(11)°	2×O–Si–O	114.27(24)°
4×Al–O	1.714(5)	4×O–Al–O	107.92(11)°	2×O–Al–O	112.62(22)°
3×Na–O	2.603(9)	3×Na–O	2.670(8)	Si–O–Al	156.17(23)°
Disordered-tilt model refinement ($Pm\bar{3}n$)					
Si	0.25	0.5	0	1	0.034(3)
Al	0.25	0	0.5	1	0.040(3)
O	0.1474(4)	0.1564(5)	0.4774(8)	0.5	0.039(1)
Na	0.2312(6)	0.2312(6)	0.2312(6)	0.375	0.042(2)
4×Si–O	1.614(5)	4×O–Si–O	106.43(12)°	2×O–Si–O	115.75(26)°
4×Al–O	1.728(5)	4×O–Al–O	107.26(11)°	2×O–Al–O	113.99(23)°
3×Na–O	2.481(7)	3×Na–O	2.778(6)	Si–O–Al	151.9(4)°
3×Na–O ^a	2.441(7)	3×Na–O ^a	2.864(8)		

^aSee text.

fit to 625 K laboratory x-ray powder diffraction data, having also tried $Im\bar{3}m$ and $I\bar{4}3m$. Their Na–O_{inner} bond length is 2.56 Å, and the average Pauling tilts calculated from their atomic coordinates are $\varphi_{\text{Si}}=4.3^\circ$ and $\varphi_{\text{Al}}=4.0^\circ$. The $P\bar{4}3n$ symmetry reflects the ordering of Al over the framework T-sites and also the nonzero Pauling tilt, but the Na–O bonds are quite long, and the Pauling tilt angles quite small. The tilt-disorder model of Behrens *et al.*³² for Ag₆–SOD employs space-group symmetry $Pm\bar{3}n$ rather than $P\bar{4}3n$, which allows the framework oxygen to move off the special (0,y,z) position onto a general position, effectively sitting on both sides of the window at half occupancy due to the disorder. The Ag⁺ is likewise allowed to sit on both sides of the window at half its normal 75% occupancy. This model provided a better fit their 723 K Ag₆–SOD XRD data and also yielded larger tilt angles ($\varphi_{\text{Si}}=14.0^\circ$, $\varphi_{\text{Al}}=13.6^\circ$) and more typical Ag–O_{inner} bond lengths (2.38 Å).

A Rietveld refinement of the structure of high-temperature cubic Na₆–SOD at 675 K was refined from our variable-temperature data XRD data. The excluded regions described for the 393 K refinement apply here as well. Both the $P\bar{4}3n$ ordered-tilt model and the $Pm\bar{3}n$ tilt-disorder model from the Ag–sodalite study of Behrens *et al.*³² were investigated. Because the *R*-factors from these two refinements were identical, the results of each are summarized in Table V. The fit to the XRD data from the tilt-disorder model refinement is shown in Fig. 11. The cell volume is only slightly larger in the high-temperature phase (a 1% increase from 393 K to 675 K), which is expected to correspond to a modest decrease in the Pauling tilt angles. Yet the $P\bar{4}3n$ refinement yields tilt angles ($\varphi_{\text{Si}}=2.9^\circ$ and $\varphi_{\text{Al}}=2.7^\circ$) that appear to have been drastically reduced relative to those at 393 K. In order to facilitate the reduction of the Pauling tilt to near zero while gaining only a small increase in volume, the Si–O and Al–O bond lengths grew short, the Si–O–Al angle straightened out to an uncharacteristically high value, and the sodium cations positions converged at uncomfortably long distances from the coordinating 6-ring oxygens, con-

firming the results of Felsche *et al.*,⁵ who reported respective Si–O and Al–O bond lengths of 1.585 Å and 1.711 Å, an Si–O–Al angle of 156.3°, and respective Na–O_{inner} and Na–O_{outer} distances of 2.56 Å and 2.69 Å.

The refinement of the $Pm\bar{3}n$ tilt-disorder model saw the oxygen shifting further away from the $z=0$ plane, resulting in larger Pauling tilt values of $\varphi_{\text{Si}}=8.8^\circ$ and $\varphi_{\text{Al}}=8.3^\circ$, which are much closer to those in the cation-ordered phase at 393 K, and also consistent with the marginal volume increase in going from 393 K to 675 K. At the same time, the Si–O and Al–O bond lengths increased to more reasonable values, the Si–O–Al angle was reduced, and the Na–O distance dropped to 2.48 Å (see Table V). The tilt-disorder model simultaneously places the Na and O atoms on both sides of the 6-ring window at half occupancy, but assumes that at any instant the local tilt will be to one side or the

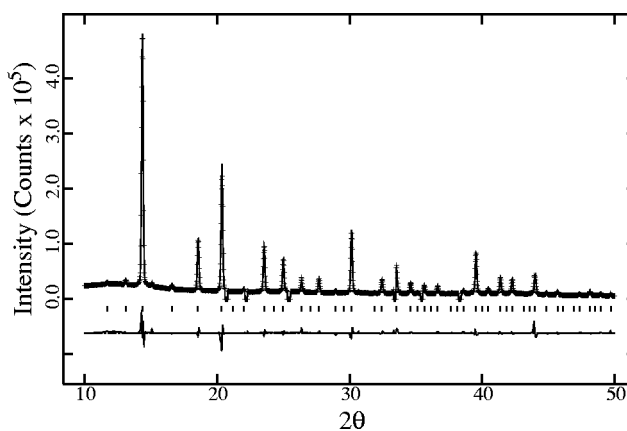


FIG. 11. Rietveld refinement of the cubic structure of Na₆–SOD at 675 K using the variable-temperature image plate XRD data and space group $P\bar{4}3n$. Refinement details: $a=9.1690(3)$ Å, $R_p=5.01\%$, $wR_p=7.55\%$, $R_B=10.73\%$, $\chi^2=110.6$, 16 refined parameters (scale factor, zero error, cell parameter, 4 isotropic thermal parameters, 4 positional parameters, and 5 profile parameters). The fit obtained using the $Pm\bar{3}n$ dynamic-tilt model refinement were very similar.

other. The bond lengths and angles from the $Pm\bar{3}n$ refinement in Table V reflect the local geometry, with the exception of the Na–O distances marked by an asterisk. These Na–O distances, which correspond to placing the Na cations on one side of the window ($+\varphi$) and the inner oxygens on the other ($-\varphi$), were included to illustrate that the cations can achieve similar coordination environments on either side of the plane formed by the window oxygens.

The abrupt onset of superlattice peaks at the cation-ordering temperature is consistent with a first-order phase transition, but the space-group symmetry of the C_{24} ordering places a firmer constraint on the nature of the transition. Using the ISOTROPY software package of Stokes and Hatch,³³ the order parameter associated with a transition from $P\bar{4}3n$ to $Pnc2$ (in the $\sqrt{2}\times\sqrt{2}\times 1$ supercell setting) was shown to belong to the $M5$ irreducible representation of $P\bar{4}3n$, after the convention of Miller and Love.³⁴ This irreducible representation allows a cubic term in the power expansion of the free energy and fails the Landau criterion for continuous phase transitions, and therefore requires such a transition to be discontinuous, whether the high-temperature phase involves one tilt direction or a disordered combination of both.

G. Analogy to oxides with anion deficient fluorite structures

Cation orderings in Na_6 –SOD are closely analogous to vacancy orderings in oxides with anion-deficient fluorite structures (OADFS's) where the anion sites form a primitive cubic lattice so that anion deficiencies are manifested as vacancies on this lattice. The OADFS anion lattice is then analogous to the sodalite cation lattice. A variety of notable vacancy-ordered OADFS's have been studied extensively, including cubic stabilized zirconia, ternary systems that combine dioxides of tetravalent metals like Th or Zr with sesquioxides of trivalent metals such as Sc or Y (e.g., $\text{Th}_{1-x}\text{Y}_x\text{O}_{2-x/2}$), and most commonly, the dioxides of the lanthanide and actinide metals (MO_{2-x}).^{35–37} The vacancy fraction (f_v) in the majority of OADFS's is considerably lower than the $f_v = 1/4$ observed in Na_6 –SOD. A notable exception is bixbyite, a mineral with composition $(\text{Mn}_{1-x}\text{Fe}_x)_2\text{O}_3$ and $x \approx 1\%$, which also has an $f_v = 1/4$ ordered-vacancy structure.³⁸ The bixbyite vacancy ordering is also observed in pure Mn_2O_3 under ambient conditions,³⁹ in addition to a small orthorhombic distortion,⁴⁰ and in sesquioxides of several other transition metals and rare earths where it is known as the C-type sesquioxide structure.³⁷ The vacancy-ordered supercell of bixbyite is cubic with cell parameter $2a$. In sodalite, looking down the $[001]$ direction, half of the cation site columns contain no vacancies, while columns with vacancies contain a vacancy in every other site. In bixbyite every column has vacancies, but only in every fourth site. The key similarity between the anion orderings in bixbyite and the low-energy cation orderings in Na_6 –SOD is the avoidance of NNV pairs. The nearest pairs of vacancies sit on opposite ends of face or body diagonals of the respective cation lattices. And for more typical OAD-

FS's with lower vacancy concentrations, even the face-diagonal vacancy pairs appear to be forbidden.

V. CONCLUSIONS

The Na_6 –SOD member of the sodalite family is much more difficult to characterize than other sodalites that do not require dehydration. Single crystals of the hydrated material shatter into very small fragments upon dehydration due to the large local strains associated with the extreme volume change that occurs as the framework responds to the removal of the water from the cages. Thus the nature of the low-temperature cation-ordering has been out of reach since the ordering transition was first reported several years ago.¹² This work has demonstrated that by combining powder diffraction methods with the results of computer simulations, several important questions can still be answered.

Though the full array of XRD superlattice peaks resisted indexing initially, an analysis of the low-temperature Bragg peak splittings revealed a pseudotetragonal supercell ($a' = \sqrt{2}a$, $b' = \sqrt{2}b$, $c' = c$) that was used to index most of the superlattice peaks in the pattern. The unindexed peaks were then shown to be accounted for by a one-dimensional 45.2 Å modulation, described by modulation vector $(211)/8.9$ in the supercell setting, that forms in cooperation with the supercell. The cation vacancy configurations native to this supercell were then enumerated, ranked according to structural energy, and judged by their ability to drive the observed pseudotetragonal distortion and to generate the correct array of superlattice peaks. In this way, C_{24} is singled out as only plausible vacancy ordering within the supercell.

From the constrained-tetrahedra refinements of the commensurate C_{24} superstructure model, the Pauling tilt was found to be significant in the cation-ordered phase, with average tilt angles of 10° at 393 K and 14° at 100 K. The decrease in tilt angle with increasing temperature is accompanied by a loss of adequate oxygen coordination at the Na(2) site. The ordered-tilt ($P\bar{4}3n$) and tilt-disorder ($Pm\bar{3}n$) models yielded essentially identical fits to the high temperature XRD data, though the tilt-disorder model led to more reasonable structural parameters.

It was not possible to establish a detailed model for the incommensurate modulation based on the XRD data alone, but because the Pauling tilt parameter of the framework TO_4 tetrahedra is active in both the high and low-temperature phases, the modulation may involve a long-period variation of the tilt angle. Such modulations are well-established in AlPO_4 ,^{41–43} and quartz,^{44–46} where large single crystals have been available, and have also been reported in aluminated sodalite systems.^{23,24} Selected area TEM diffraction data from a small particle would allow one to determine the (3 + 1)-dimensional incommensurate superspace group symmetry⁴⁷ if systematic absences could be adequately identified. A full Rietveld refinement of the modulated structure using a software package such as XND (Ref. 48) or PREMOS (Ref. 49) might then be within reach.

ACKNOWLEDGMENTS

Special thanks to David Cox and Jonathan Hanson at BNL for assistance with the x-ray data collection, and to Vojislav Srdanov (U.C. Santa Barbara), Harold Stokes (Brigham Young U.) and Sander van Smaalen (U. Bayreuth, Germany) for helpful discussions and insights. We acknowledge grant support from the MRSEC Program of the National Science Foundation, No. DMR96-32716 (B.J.C., J.M.D., A.K.C., G.D.S.), the National Science Foundation, No. CHE97-09038 (N.P.B., S.R.S.), and the Office of Naval Research, Nos. N00014-99-1-0624 (N.P.B., S.R.S.) and N00014-99-1-0266 (B.B.I., S.L., G.D.S.). Work at the BNL NSLS beamlines X7A and X7B was supported under Contracts Nos. AC02-98 CH10886 and AC02-76CH00016 of the U.S. DOE, Office of Basic Energy Sciences.

- ¹L. Pauling, *Z. Kristallogr.* **74**, 213 (1930).
- ²W. Loewenstein, *Am. Mineral.* **39**, 92 (1954).
- ³An expression coined by V. I. Srdanov.
- ⁴J. Felsche and S. Luger, *Ber. Bunsenges. Phys. Chem.* **90**, 731 (1986).
- ⁵J. Felsche, S. Luger, and Ch. Baerlocher, *Zeolites* **6**, 367 (1986).
- ⁶A. Stein, M. Meszaros, P. M. MacDonald, G. A. Ozin, and G. D. Stucky, *Adv. Mater.* **3**, 306 (1991).
- ⁷A. Stein, G. A. Ozin, P. M. MacDonald, and G. D. Stucky, *J. Am. Chem. Soc.* **114**, 5171 (1992).
- ⁸S. E. Lattner, J. Sachleben, B. B. Iversen, J. Hansen, and G. D. Stucky, *J. Phys. Chem. B* **103**, 7135 (1999).
- ⁹G. K. H. Madsen, C. Gatti, B. B. Iversen, L. Damjanovic, G. D. Stucky, and V. I. Srdanov, *Phys. Rev. B* **59**, 12359 (1999).
- ¹⁰I. Hassan and H. D. Grundy, *Acta Crystallogr., Sect. B: Struct. Sci.* **40**, 6 (1984).
- ¹¹W. Depmeier, *Acta Crystallogr., Sect. B: Struct. Sci.* **40**, 185 (1984).
- ¹²P. Sieger, Ph.D. Dissertation, Constance, Germany, Hartung-Gorre-Verlag, ISBN 3891915934, 1992.
- ¹³W. Depmeier, *Z. Kristallogr.* **199**, 75 (1992).
- ¹⁴W. Depmeier, *Acta Crystallogr., Sect. B: Struct. Sci.* **44**, 201 (1988).
- ¹⁵S. R. Shannon, B. J. Campbell, H. Metiu, and N. P. Blake, *J. Chem. Phys.* **113**, 10215 (2000), preceding paper.
- ¹⁶P. Norby, *J. Appl. Crystallogr.* **30**, 21 (1997).
- ¹⁷A. C. Larson and R. B. Von Dreele, *GSAS Manual*, Los Alamos Report No. LAUR-86-748, 1986, Los Alamos National Laboratory, New Mexico.
- ¹⁸S. van Smaalen, R. Dinnebier, H. Katzke, and W. Depmeier, *J. Solid State Chem.* **129**, 130 (1997).
- ¹⁹P. Thompson, D. E. Cox, and J. B. Hastings, *J. Appl. Crystallogr.* **20**, 79 (1987).
- ²⁰L. W. Finger, D. E. Cox, and A. P. Jephcoat, *J. Appl. Crystallogr.* **27**, 892 (1994).
- ²¹Y. Billiet and E. F. Bertaut, in *International Tables of Crystallography*, 3rd ed., edited by Theo Hahn (Kluwer Academic, New York, 1992), ISBN 0792316789, Vol. A, Chap. 13.
- ²²C. Wilkinson, G. Lautenschlager, R. Hock, and H. Weitzel, *J. Appl. Crystallogr.* **24**, 365 (1991).
- ²³D. M. Tobbens and W. Depmeier, *Z. Kristallogr.* **213**, 52 (1998).
- ²⁴W. Depmeier, *J. Alloys Compd.* **188**, 21 (1992).
- ²⁵J. L. Schlenke, J. J. Pluth, and J. V. Smith, *Mater. Res. Bull.* **14**, 751 (1979).
- ²⁶H. Katzke, M. Czank, W. Depmeier, and S. van Smaalen, *J. Phys.: Condens. Matter* **9**, 6231 (1997).
- ²⁷A. M. Panich, *J. Phys. Chem. Solids* **57**, 1031 (1995).
- ²⁸*Atlas of Zeolite Structures*, 3rd ed., edited by W. M. Meier and D. H. Olson (Butterworth-Heinemann, London, 1992), ISBN 0750693312.
- ²⁹InsightII software package, Molecular Simulations Incorporated, San Diego, CA.
- ³⁰N. P. Blake, P. C. Weakliem, and H. Metiu, *J. Phys. Chem. B* **102**, 67 (1998).
- ³¹A. F. Jensen, F. K. Larsen, B. B. Iversen, V. Petricek, T. Schultz, and Y. Gao, *Acta Crystallogr., Sect. B: Struct. Sci.* **53**, 113 (1997).
- ³²P. Behrens, P. B. Kempa, S. Assmann, M. Wiebcke, and J. Felsche, *J. Solid State Chem.* **115**, 55 (1995).
- ³³H. T. Stokes and D. M. Hatch, *Isotropy Subgroups of the 230 Crystallographic Space Groups* (World Scientific, Singapore, 1988); H. T. Stokes and D. M. Hatch, ISOTROPY computer program, www.physics.byu.edu/~stokesh/isotropy.html.
- ³⁴S. C. Miller and W. F. Love, *Tables of Irreducible Representations of the Space Groups and Co-Representations of Magnetic Space Groups* (Pruett, Boulder, 1977).
- ³⁵A. K. Cheetham, in *Nonstoichiometric Oxides*, edited by O. T. Sorensen (Academic, New York, 1981), ISBN 0126552800, pp. 399–433, and references therein.
- ³⁶A. F. Wells, *Structural Inorganic Chemistry*, 4th ed. (Clarendon, Oxford, 1975), ISBN 0198553544.
- ³⁷J. Zhang, R. B. Von Dreele, and L. Eyring, *J. Solid State Chem.* **104**, 21 (1993); **118**, 133 (1995); **118**, 141 (1995); **122**, 53 (1996).
- ³⁸W. Zachariasen, *Z. Kristallogr.* **67**, 425 (1928).
- ³⁹L. Pauling and M. D. Shappell, *Z. Kristallogr.* **75**, 128 (1930).
- ⁴⁰S. Geller, *Acta Crystallogr., Sect. B: Struct. Crystallogr. Cryst. Chem.* **27**, 821 (1971).
- ⁴¹G. van Tendeloo, J. van Landuyt, and S. Amelinckx, *Phys. Status Solidi A* **30**, K11 (1975); **33**, 723 (1976).
- ⁴²J. P. Bacheimer, B. Berge, G. Dolino, P. Saint-Gregorie, and C. M. E. Zeyen, *Solid State Commun.* **51**, 55 (1984).
- ⁴³E. Snoeck, H. Mutka, and C. Roncan, *J. Phys. (Paris)* **50**, 56 (1989).
- ⁴⁴G. Dolino, J. P. Bacheimer, B. Berge, and C. M. E. Zeyen, *J. Phys. (Paris)* **45**, 361 (1984).
- ⁴⁵B. Berge, G. Dolino, M. Vallade, M. Boissier, and R. Vacher, *J. Phys. (Paris)* **45**, 715 (1984).
- ⁴⁶G. Dolino, J. P. Bacheimer, B. Berge, C. M. E. Zeyen, G. van Tendeloo, J. van Landuyt, and S. Amelinckx, *J. Phys. (Paris)* **45**, 901 (1984).
- ⁴⁷P. M. de Wolff, T. Janssen, and A. Janner, *Acta Crystallogr., Sect. A: Cryst. Phys., Diffr., Theor. Gen. Crystallogr.* **37**, 625 (1981).
- ⁴⁸XND software package, J. F. Bézar, Laboratoire de Cristallographie-CNRS, Grenoble, France.
- ⁴⁹PREMOS software package, A. Yamamoto, National Institute for Research in Inorganic Materials, Ibaraki, Japan.